Kinetic Modeling of the Tau PET Tracer ^{18}F-AV-1451 in Human Healthy Volunteers and Alzheimer Disease Subjects

Olivier Barret[1], David Alagille[1], Sandra Sanabria[2], Robert A. Comley[3], Robby M. Weimer[2], Edilio Borroni[3], Mark Mintun[4], Nicholas Seneca[5], Caroline Papin[1], Thomas Morley[1], Ken Marek[1], John P. Seibyl[1], Gilles D. Tamagnan[1], and Danna Jennings[1]

[1]Molecular NeuroImaging LLC, New Haven, Connecticut; [2]Genentech Research and Early Development, Genentech, South San Francisco, California; [3]Pharma Research and Early Development, F. Hoffmann-La Roche, Konzern-Hauptsitz, Basel, Switzerland; [4]Avid Radiopharmaceuticals, Philadelphia, Pennsylvania; and [5]Product Development, F. Hoffmann-La Roche, Konzern-Hauptsitz, Basel, Switzerland

^{18}F-AV-1451 is currently the most widely used of several experimental tau PET tracers. The objective of this study was to evaluate ^{18}F-AV-1451 binding with full kinetic analysis using a metabolite-corrected arterial input function and to compare parameters derived from kinetic analysis with SUV ratio (SUVR) calculated over different imaging time intervals. **Methods:** ^{18}F-AV-1451 PET brain imaging was completed in 16 subjects: 4 young healthy volunteers (YHV), 4 aged healthy volunteers (AHV), and 8 Alzheimer disease (AD) subjects. Subjects were imaged for 3.5 h, with arterial blood samples obtained throughout. PET data were analyzed using plasma and reference tissue–based methods to estimate the distribution volume, binding potential (BP_{ND}), and SUVR. BP_{ND} and SUVR were calculated using the cerebellar cortex as a reference region and were compared across the different methods and across the 3 groups (YHV, AHV, and AD). **Results:** AD demonstrated increased ^{18}F-AV-1451 retention compared with YHV and AHV based on both invasive and noninvasive analyses in cortical regions in which paired helical filament tau accumulation is expected in AD. A correlation of $R^2 > 0.93$ was found between BP_{ND} (130 min) and SUVR-1 at all time intervals. Cortical SUVR curves reached a relative plateau around 1.0–1.2 for YHV and AHV by approximately 50 min, but increased in AD by up to approximately 20% at 110–130 min and approximately 30% at 160–180 min relative to 80–100 min. Distribution volume (130 min) was lower by 30%–35% in the YHV than AHV. **Conclusion:** Our data suggest that although ^{18}F-AV-1451 SUVR curves do not reach a plateau and are still increasing in AD, an SUVR calculated over an imaging window of 80–100 min (as currently used in clinical studies) provides estimates of paired helical filament tau burden in good correlation with BP_{ND}, whereas SUVR sensitivity to regional cerebral blood changes needs further investigation.

Key Words: tau protein; Alzheimer; PET; ^{18}F-AV-1451; kinetic modeling

J Nucl Med 2017; 58:1124–1131
DOI: 10.2967/jnumed.116.182881

The accumulation of folded hyperphosphorylated tau is 1 pathologic hallmark for Alzheimer disease (AD) and forms the basis of the neuropathologic staging of Alzheimer-related pathology in the brain (*1*). ^{18}F-AV-1451 (^{18}F-T807, flortaucipir) (*2*) is a PET radiotracer with high affinity and specificity for tau aggregates, while lacking affinity for concomitant amyloid-β plaques in human AD (*3,4*). Several additional PET agents have been proposed for the imaging of tau in the brain, in particular ^{11}C-PBB3 (*5,6*), ^{18}F-THK-5117 (*7*), ^{18}F-T808 (*8*), ^{18}F-PI-2014 (*9*), and more recently ^{11}C-RO6924963, ^{11}C-RO6931643, ^{18}F-RO6958948 (*10*), ^{18}F-THK-5351 (*11*), ^{18}F-GTP1 (*12*), and ^{18}F-MK6240 (*13*), and have been or are being characterized and evaluated in humans. Currently, ^{18}F-AV-1451 has been the most widely used and characterized PET tracer (*2–4,14,15*) in clinical studies. Early clinical evaluation has demonstrated heterogeneous and asymmetric brain uptake of the radiotracer (*2*) consistent with the earlier reports by Braak and Braak (*1*) showing distribution of tau that follows discrete patterns in cross-sectional postmortem analyses generally correlating with AD severity.

Validation of a quantitative PET outcome measure for ^{18}F-AV-1451 is necessary to address questions relevant to drug development and the primary pathophysiology of AD. SUV ratio (SUVR) has been widely used as a semiquantitative outcome measure, because it can be obtained using simplified methods of acquisition and analysis. Quantification using this method may be influenced by confounding factors such that assessment of ^{18}F-AV-1451 signal or longitudinal changes of signal may not solely reflect the actual tau density in brain tissue.

In this report, we have compared the validity of SUVR to more robust quantitative measurements obtained through kinetic modeling of the PET data. Recently, SUVR was compared with a tissue-based method (*15*). In this study, an arterial input function corrected for metabolites was obtained in both healthy volunteers (HV) and subjects with AD, and classic pharmacokinetic modeling of the ^{18}F-AV-1451 PET data using plasma-based or tissue-based methods was performed.

MATERIALS AND METHODS

Radiochemistry

Radiolabeling and preparation of ^{18}F-AV-1451 was described previously (*16*). All productions showed a radiochemical purity above 99% and specific activity exceeding 200 GBq/μmol. The average decay-corrected radiochemical yield was 15.4% ± 5.5% (n = 16) in 60 min.

Human Subjects

Sixteen subjects were enrolled and completed ^{18}F-AV-1451 brain PET studies: 4 young healthy volunteers (YHV) (age, 26–37 y), 4 aged healthy

Received Aug. 19, 2016; revision accepted Nov. 22, 2016.
For correspondence or reprints contact: Olivier Barret, Molecular NeuroImaging, LLC, 60 Temple St., Suite 8B, New Haven, CT 06510.
E-mail: obarret@mnimaging.com
Published online Dec. 1, 2016.

volunteers (AHV) (age, 51–72 y), and 8 AD subjects (age, 57–85 y; Mini-Mental State Examination, 14–29) (Table 1). All subjects gave their written informed consent before participation in this study. The study protocol was reviewed and approved by the New England Institutional Review Board. The study was registered on ClinicalTrials.gov (NCT02370524).

Individuals with mild and moderate AD were required to meet the criteria based on the National Institute of Neurologic and Communicative Disorders and Stroke/Alzheimer Disease and Related Disorders Association and Diagnostic and Statistical Manual of Mental Disorders (*17*) for study eligibility. All HVs were required to have no evidence of cognitive impairment or early dementia as judged by the investigator. AHVs and AD subjects underwent ^{18}F-florbetapir amyloid imaging at screening and required a visual analysis positive for AD (*18*) and negative for AHV.

Brain PET Studies

PET images were acquired on an ECAT EXACT HR+ camera (Siemens). Subjects were administered intravenously a single dose of ^{18}F-AV-1451 (Table 1) over 2 min, followed by a 10-mL saline flush.

Dynamic 3-dimensional brain PET images were acquired over 210 min as 3 imaging sessions of 50 min each (0–50, 80–130, and 160–210 min) with 30-min breaks between sessions. The first session consisted of 21 frames (6×0.5, 4×1, 4×2, 7×5 min), and the second and third sessions consisted of 10 frames (10×5 min). A ^{68}Ge rod source transmission scan was obtained before each emission for attenuation correction. PET data were corrected for randoms, dead time, scatter, and attenuation, and PET images were reconstructed using ordered-subset expectation maximization algorithm (4 iterations, 16 subsets, 5-mm gaussian postprocessing filter).

A structural 3-dimensional T1-weighted MR image was acquired for all subjects on a Espree 1.5-T scanner (Siemens) (magnetization-prepared rapid gradient-echo; inversion time, 1.1 s; repetition time, 1.97 s; echo time, 3.17 ms; flip angle, 15°).

Blood Sampling and Analysis

Arterial blood samples were collected throughout the 210 min of acquisition (every 30 s until 4 min after injection with decreasing frequency thereafter) and whole blood and plasma radioactivity measured in a well-type γ-counter (Wallac 2480; Perkin Elmer). Radiometabolites were measured in a subset of samples (4, 8, 15, 30, 60, 90, 130, 170, and 210 min) by reversed-phase high-performance liquid chromatography, and plasma protein binding free fraction was measured by ultrafiltration (Centrifree; Millipore).

The parent fraction profile was fitted with a monoexponential plus constant function using measurements up to 130 min (last 2 samples at 170 and 210 min suffered from low count statistics and were excluded from the fit), and extrapolated thereafter. The arterial plasma concentration curve was time multiplied by the fitted curve to correct for radiometabolites.

Image Processing and Analysis

Images were analyzed in PMOD 3.607 software (PMOD Technologies). All realignment procedures used normalized mutual information. PET images were motion-corrected within and between imaging sessions by realigning each image to the initial flowlike (15 min) average image. The subject MR image was segmented into gray and white matter maps. The initial flowlike average PET image was used to align the whole PET series onto the MR image, and subsequently both MRI and PET series were spatially normalized to the standard Montreal Neurologic Institute space. Hammers volume-of-interest atlas (*19*) was applied to normalized PET images, and time–activity curves were extracted for the following brain regions (left- and right-side regions separately): frontal (middle, inferior, superior), parietal, occipital, temporal (superior lateral, inferior lateral, mesial), putamen, caudate nucleus, globus pallidus, thalamus as well as cerebellar cortex, with cortical and cerebellar cortex regions constrained to gray matter voxels. The cerebellar cortex region was eroded away from other regions by 8 mm to minimize spill-over, in particular from the temporal and occipital regions.

The standard 2-tissue-compartment model (2T), 1-tissue-compartment model (1T), and Logan graphical analysis (LGA; $t^* = 80$ min) plasma-based methods were used with the radiometabolite-corrected arterial plasma input function to estimate distribution volume (V_T) in specific brain regions (*20,21*). 1T and 2T used a fixed blood volume of 5%. The binding potential (BP_{ND}) was calculated indirectly as $(V_T - V_{ND})/V_{ND}$, where V_{ND} is the nondisplaceable volume of distribution as estimated in the cerebellar cortex. The noninvasive simplified reference tissue model (SRTM) (*22*) and noninvasive LGA (NI-LGA; $k_2' = 0.05$ min^{-1}, $t^* = 80$ min) (*21*) were used to determine directly BP_{ND} using the cerebellar cortex as the reference region. For NI-LGA, k_2' was fixed to the average value across regions and subjects of k_2' calculated with SRTM. V_T and

TABLE 1
Demographics and Clinical Characteristics

Characteristic	YHV	AHV	AD subject
No. (% male)	4 (50%)	4 (50%)	8 (38%)
Age (y)	31.8 ± 4.5 (26–37)	62.5 ± 9.4 (51–72)	64.9 ± 8.6 (57–85)
MMSE	30.0 ± 0.0 (30)	29.5 ± 0.6 (29–30)	22.4 ± 5.5 (14–29)
CDR-SB	NA	NA	0.8 ± 0.3 (0.5–1)
ADAS-cog	NA	NA	20.6 ± 10.2 (4–30)
^{18}F-AV-1451 (MBq)	303.3 ± 33.2 (259.6–340.4)	341.3 ± 2.5 (338.5–344.5)	341.3 ± 11.7 (325.4–357.0)
AV-1451 (μg)	0.49 ± 0.13 (0.38–0.67)	0.82 ± 0.59 (0.16–1.49)	0.58 ± 0.46 (0.11–1.55)
^{18}F-florbetapir SUVR	NA	1.19 ± 0.04	1.46 ± 0.31

MMSE = Mini-Mental State Examination; CDR-SB = Clinical Dementia Rating, sum of boxes; NA = not applicable; ADAS-cog = Alzheimer Disease Assessment Scale-Cognition.

Values are mean ± SD, with range in parentheses. Cerebellar cortex was used as reference; average of frontal, parietal, temporal, anterior, and posterior cingulated cortex.

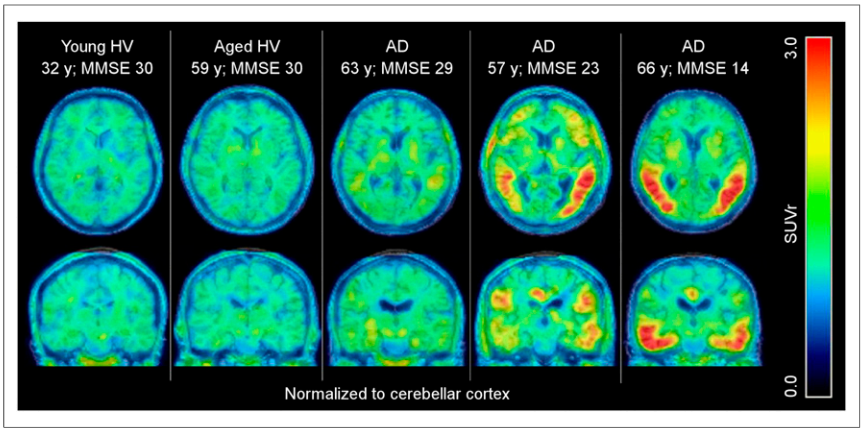

FIGURE 1. ^{18}F-AV-1451 SUVR images (80–100 min) superimposed onto subject's MR image in transaxial (top row) and coronal (bottom row) views in 1 YHV, 1 AHV, and 3 AD subjects.

BP_{ND} were estimated for 130 min (first 2 imaging sessions) and 210 min of data (whole acquisition), and unless specified otherwise the reported results are for 130 min due to the increased input function uncertainty and PET data noise at later times.

SUVs were calculated by normalizing the uptake values by the injected dose divided by the subject weight. Target–to–cerebellar cortex SUVRs were calculated for 4 time intervals (80–100, 110–130, 160–180, and 190–210 min) and compared with BP_{ND}.

RESULTS

Representative average ^{18}F-AV-1451 SUVR images (80–100 min) are shown in Figure 1 for 1 YHV, 1 AHV, and 3 AD subjects, visually demonstrating increased retention in AD compared with HV. Time–activity and SUVR curves are shown in Figure 2 for 1 YHV, 1 AHV, and 1 AD subject. YHVs and AHVs display rapid uptake and clearance of the tracer across all brain regions, with putamen uptake slightly elevated initially in YHVs and clearly elevated in AHVs. Retention of the tracer was observed in AD in cortical regions with noticeable region-specific and asymmetrical signal, with further elevated putamen uptake exhibiting different kinetics compared with cortical regions with high initial uptake and much faster clearance. Pseudoequilibrium was not reached at 210 min after injection with SUVR curves still increasing. Additional across-subject comparison of SUVR curves per region are provided in Supplemental Figures 1–6 (supplemental materials are available at http://jnm.snmjournals.org).

Moderately fast metabolism of ^{18}F-AV-1451 was observed (Fig. 3A), with 2 main radiometabolites much more polar than the parent. At 90 min after radiotracer injection, the parent fraction in arterial plasma was 17.3% ± 7.0% across all subjects (n = 16). No difference was observed among the 3 groups. The free fraction in plasma was low at 0.19% ± 0.12% (n = 16). The average metabolite-corrected arterial plasma is also shown in Figure 3B.

Examples of fits/linear regression for 210 min of data are shown in Figure 4 for an AD subject. 2T described adequately the data up to 210 min. 1T gave poor fits for all subjects and regions, including the cerebellar cortex (data not shown) and is

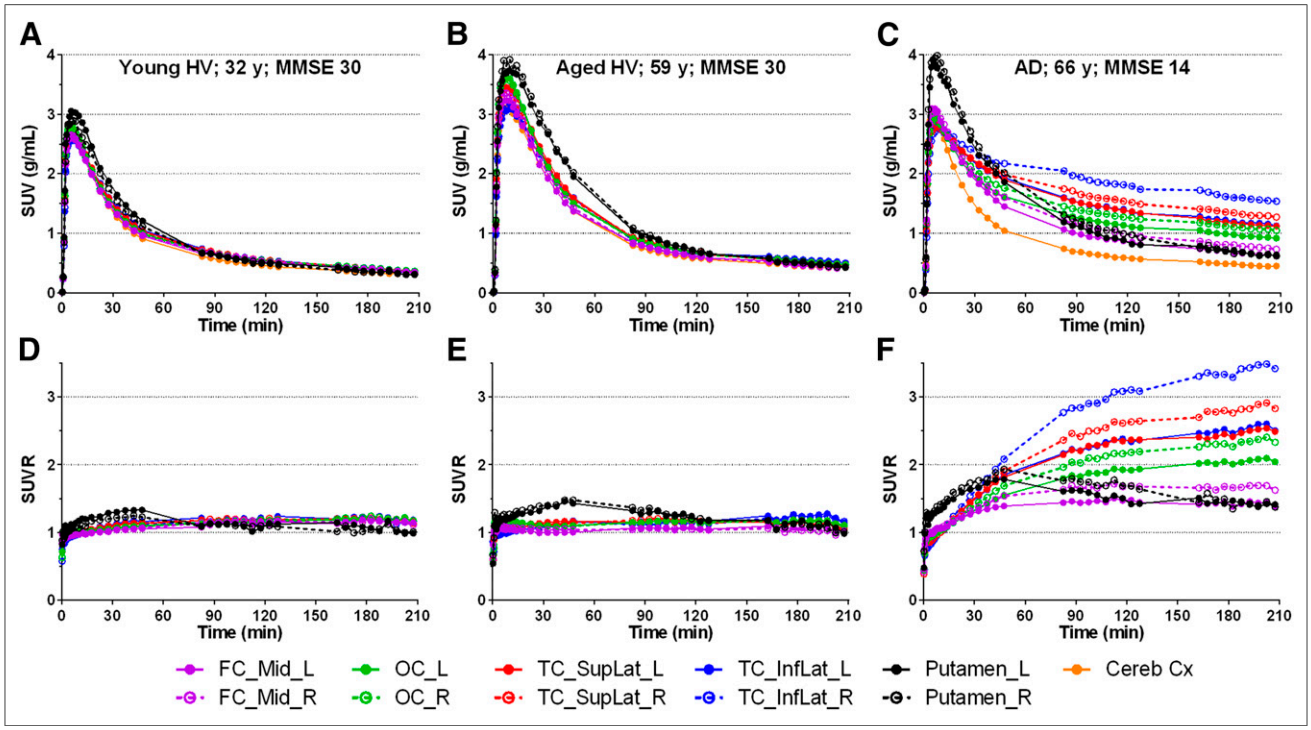

FIGURE 2. ^{18}F-AV-1451 time–activity and SUVR curves in YHV (A and D), AHV (B and E), and AD subject (C and F). Closed symbols and solid lines = left side; open symbols and dashed lines = right side; cereb Cx = cerebellar cortex; FC_Mid = frontal middle cortex; OC = occipital cortex; TC_InfLat = inferior lateral temporal cortex; TC_SupLat = superior lateral temporal cortex.

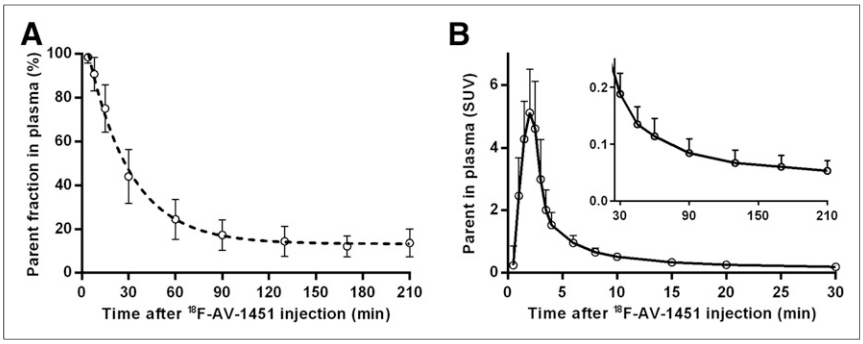

FIGURE 3. (A) Average (mean ± SD) parent fraction profile in arterial plasma after intravenous administration of ^{18}F-AV-1451. Dashed line represents monoexponetial plus constant fit up to 130 min. (B) Average (mean ± SD) radiometabolite-corrected arterial plasma concentration of ^{18}F-AV-1451 (input function).

not reported further. LGA or NI-LGA plots are close to linearity for the last 2 imaging sessions. SRTM did not describe the data as well over 210 min, with some convergence or fit difficulties in some regions while showing excellent agreement with NI-LGA ($R^2 > 0.99$, linear regression on top of identity line), and is therefore not reported further.

Detailed results of the 2T analysis are given in Table 2 and Figure 5. K_1 was regionally different, highest in the putamen, but appeared similar in YHVs and AHVs in all regions (within ~3%) and across the 3 groups in the cerebellar cortex and putamen, whereas it was lower by approximately 10%–15% in the cortical regions of AD subjects, similar to previous findings (*23*). K_1/k_2 was clearly lower by about 30% in YHVs including in the cerebellar cortex (2.7 mL/cm^3) compared with AHVs (3.9 mL/cm^3) and AD subjects (3.7 mL/cm^3). V_T was elevated in the cortical regions of AD subjects (as expected) but similar between AHVs and AD subjects in the cerebellum (6.0 and 5.9 mL/cm^3, respectively), whereas it was noticeably lower by again 30%–35% in YHVs, with 4.1 mL/cm^3 for the cerebellar cortex. A regression analysis (Fig. 6) showed a correlation between V_T and the subject's age, with an R^2 greater than 0.87 ($n = 8$, YHV and AHV) and a higher increase with age in the putamen (slope of ~0.095) compared with other regions (slope of ~0.06–0.08). K_1 and V_T were well identified, with parameter errors of 2%–4%. The identifiability for k_2 was decreased (error up to ~7%), but the ratio K_1/k_2 maintained an acceptable error of approximately 4%, except in the mesial temporal and putamen. k_3 and k_4 were not well identified (errors up to ~25%), in particular for k_3 in the mesial temporal and putamen (30%–35%), whereas k_3/k_4 was better defined (~10%), except in the mesial temporal and putamen (15%–25%), where the increased errors in these regions is likely caused by higher correlation between k_2 and k_3 (*24*).

Results of BP_{ND} and SUVR are summarized in Supplemental Table 1, and correlation analyses between these measurements in cortical regions (AD only) are provided in Table 3 and shown in Figure 7. Overall, a good correlation was found between all methods and scan durations with an R^2 greater than 0.96. LGA and NI-LGA underestimated BP_{ND} by approximately 10% and 20%, respectively, compared with 2T. The agreement between 2T and SUVR-1 in terms of R^2 was similar for 80–100 min and 110–130 min, whereas it was slightly better for 110–130 min when compared with LGA or NI-LGA estimates, although when additionally considering a slope closer to unity and a smaller bias (introduced through the intercept) the 110- to 130-min interval performed better. Within-method comparison showed a time-dependency of the estimates, with BP_{ND} increasing by 15%, 10%, and 12% for 2T, LGA, and NI-LGA, respectively, and V_T increasing by about 20% for both 2T and LGA (with a higher R^2 for the graphical methods) when using 210 min of data, likely because of nonequilibrium between plasma and brain regions. LGA V_T correlated strongly with 2T ($R^2 > 0.98$), with, however, an underestimation of about 5%.

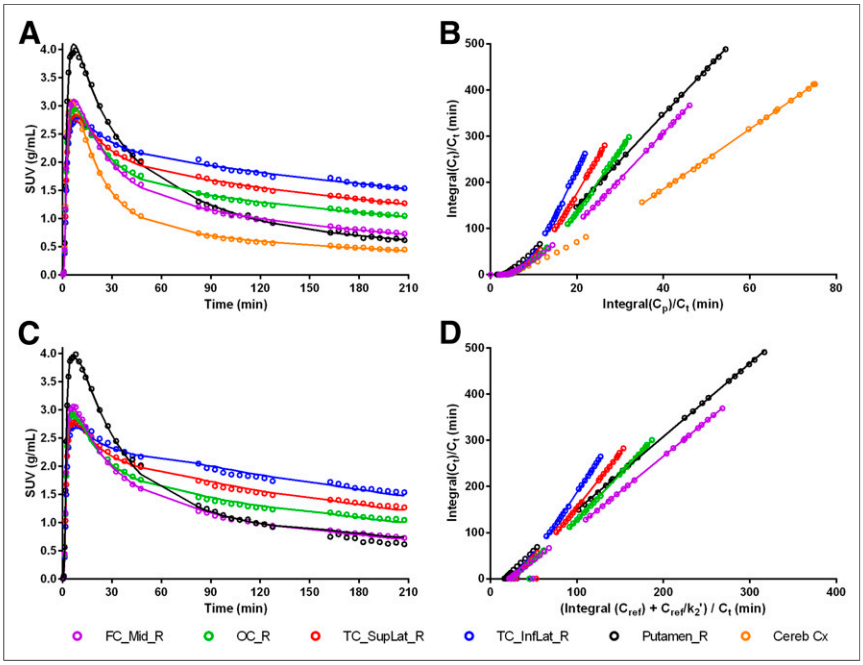

FIGURE 4. Compartmental and graphical analysis for AD for 210 min of scanning data: 2T fits (A), LGA linear regression (B), SRTM fits (C), and noninvasive LGA linear regression (D). Open symbols = measured data; solid lines = fitted curve/line; Cereb Cx = cerebellar cortex; FC_Mid = frontal middle cortex; OC = occipital cortex; TC_InfLat = inferior lateral temporal cortex; TC_SupLat = superior lateral temporal cortex.

DISCUSSION

We report the kinetic analysis of ^{18}F-AV-1451 using an arterial input function to evaluate its pharmacokinetic properties in the brain. AD demonstrated increased ^{18}F-AV-1451 retention compared with HV visually in cortical regions in which paired helical filament tau accumulation is expected in AD, as well as quantitatively based invasive (2T and LGA) and noninvasive (NI-LGA

TABLE 2
Estimates of 2T Parameters and Macroparameters Using 130 Minutes of Scanning Data

Parameter	Group	Frontal	Parietal	Occipital	Lateral temporal	Mesial temporal	Putamen	Cerebellar cortex
K_1	YHV	0.28 ± 0.06 (3% ± 1%)	0.29 ± 0.06 (3% ± 1%)	0.30 ± 0.07 (3% ± 1%)	0.27 ± 0.06 (3% ± 1%)	0.21 ± 0.04 (4% ± 0%)	0.35 ± 0.08 (5% ± 1%)	0.30 ± 0.07 (3% ± 1%)
	AHV	0.29 ± 0.03 (3% ± 1%)	0.31 ± 0.03 (3% ± 1%)	0.31 ± 0.03 (2% ± 1%)	0.28 ± 0.04 (2% ± 1%)	0.21 ± 0.02 (3% ± 1%)	0.35 ± 0.03 (3% ± 0%)	0.29 ± 0.03 (2% ± 1%)
	AD	0.25 ± 0.03 (2% ± 1%)	0.25 ± 0.04 (2% ± 1%)	0.28 ± 0.05 (2% ± 1%)	0.24 ± 0.04 (2% ± 1%)	0.20 ± 0.02 (2% ± 1%)	0.35 ± 0.06 (3% ± 2%)	0.29 ± 0.03 (2% ± 1%)
K_1/k_2	YHV	2.69 ± 0.55 (4% ± 1%)	2.69 ± 0.57 (4% ± 0%)	2.81 ± 0.54 (4% ± 0%)	2.89 ± 0.58 (5% ± 0%)	2.53 ± 0.69 (8% ± 3%)	2.82 ± 0.64 (12% ± 8%)	2.72 ± 0.63 (4% ± 0%)
	AHV	3.94 ± 0.26 (4% ± 1%)	4.08 ± 0.21 (4% ± 1%)	4.21 ± 0.26 (3% ± 1%)	4.35 ± 0.26 (4% ± 1%)	3.78 ± 0.41 (6% ± 2%)	4.82 ± 0.88 (8% ± 2%)	3.95 ± 0.26 (4% ± 1%)
	AD	3.73 ± 0.50 (4% ± 2%)	3.67 ± 0.34 (4% ± 2%)	3.82 ± 0.38 (4% ± 1%)	4.17 ± 0.59 (5% ± 2%)	3.73 ± 0.46 (6% ± 3%)	4.30 ± 1.34 (9% ± 6%)	3.69 ± 0.53 (3% ± 2%)
k_4	YHV	0.023 ± 0.010 (17% ± 6%)	0.023 ± 0.009 (15% ± 5%)	0.022 ± 0.007 (16% ± 4%)	0.026 ± 0.010 (17% ± 6%)	0.032 ± 0.019 (19% ± 8%)	0.068 ± 0.044 (15% ± 4%)	0.029 ± 0.014 (18% ± 6%)
	AHV	0.017 ± 0.005 (22% ± 6%)	0.017 ± 0.004 (21% ± 3%)	0.014 ± 0.004 (21% ± 3%)	0.017 ± 0.005 (23% ± 5%)	0.020 ± 0.010 (27% ± 12%)	0.041 ± 0.018 (19% ± 18%)	0.019 ± 0.007 (21% ± 5%)
	AD	0.022 ± 0.010 (11% ± 8%)	0.020 ± 0.008 (9% ± 5%)	0.018 ± 0.008 (10% ± 7%)	0.020 ± 0.009 (13% ± 9%)	0.021 ± 0.008 (16% ± 10%)	0.044 ± 0.018 (10% ± 6%)	0.027 ± 0.010 (12% ± 8%)
k_3/k_4	YHV	0.69 ± 0.16 (10% ± 2%)	0.73 ± 0.18 (9% ± 2%)	0.69 ± 0.19 (9% ± 2%)	0.65 ± 0.15 (11% ± 2%)	0.83 ± 0.33 (15% ± 5%)	0.77 ± 0.38 (26% ± 11%)	0.54 ± 0.14 (12% ± 3%)
	AHV	0.61 ± 0.12 (9% ± 2%)	0.64 ± 0.10 (8% ± 1%)	0.72 ± 0.15 (8% ± 2%)	0.63 ± 0.12 (10% ± 3%)	0.71 ± 0.11 (17% ± 6%)	0.65 ± 0.16 (21% ± 2%)	0.51 ± 0.05 (9% ± 3%)
	AD	1.16 ± 0.65 (8% ± 5%)	1.36 ± 0.73 (7% ± 4%)	1.41 ± 0.89 (7% ± 4%)	1.32 ± 0.76 (9% ± 5%)	1.15 ± 0.54 (11% ± 6%)	1.17 ± 0.89 (16% ± 7%)	0.62 ± 0.20 (9% ± 4%)
$K_1k_3/$	YHV	1.79 ± 0.21 (7% ± 1%)	1.89 ± 0.18 (6% ± 1%)	1.88 ± 0.25 (6% ± 1%)	1.82 ± 0.17 (8% ± 1%)	1.91 ± 0.23 (9% ± 2%)	2.03 ± 0.74 (14% ± 4%)	1.42 ± 0.10 (9% ± 1%)
k_2k_4	AHV	2.43 ± 0.55 (7% ± 3%)	2.61 ± 0.46 (7% ± 2%)	3.05 ± 0.75 (7% ± 4%)	2.77 ± 0.58 (8% ± 4%)	2.71 ± 0.55 (12% ± 9%)	3.01 ± 0.43 (14% ± 4%)	2.03 ± 0.33 (7% ± 1%)
	AD	4.32 ± 2.70 (5% ± 4%)	4.90 ± 2.60 (4% ± 2%)	5.34 ± 3.47 (5% ± 3%)	5.44 ± 3.30 (6% ± 5%)	4.27 ± 2.18 (6% ± 4%)	4.03 ± 1.12 (8% ± 3%)	2.25 ± 0.71 (5% ± 3%)
V_T	YHV	4.49 ± 0.62 (3% ± 2%)	4.58 ± 0.60 (2% ± 1%)	4.68 ± 0.57 (2% ± 1%)	4.72 ± 0.58 (2% ± 2%)	4.45 ± 0.58 (2% ± 2%)	4.85 ± 0.76 (1% ± 0%)	4.14 ± 0.64 (2% ± 2%)
	AHV	6.37 ± 0.73 (3% ± 2%)	6.69 ± 0.62 (3% ± 1%)	7.26 ± 0.95 (4% ± 2%)	7.12 ± 0.78 (4% ± 2%)	6.48 ± 0.89 (5% ± 5%)	7.84 ± 0.81 (2% ± 2%)	5.98 ± 0.58 (2% ± 1%)
	AD	8.05 ± 2.85 (2% ± 2%)	8.58 ± 2.52 (2% ± 1%)	9.16 ± 3.48 (2% ± 1%)	9.62 ± 3.42 (2% ± 2%)	8.00 ± 2.29 (3% ± 2%)	8.34 ± 0.92 (1% ± 0%)	5.94 ± 0.85 (1% ± 0%)

Rate constants and macroparameters are presented as mean ± SD and SEs are expressed as percentage and reported as mean ± SD. Average of left and right regions; frontal = average of inferior, superior, and middle; lateral temporal = average of superior and inferior.

and SUVR) analyses. Subjects with presumed negligible or low tau exhibited evidence of equilibration with constant tissue ratios attained, whereas those with presumed substantial tau showed steady accumulation beyond 210 min. Despite these kinetic characteristics, a comparison between the invasive 2T and SUVR showed a strong linear correlation ($R^2 > 0.96$) between BP_{ND} and SUVR-1 across subjects and across regions. Both imaging time intervals of 80–100 min and 110–130 min gave comparable results, in agreement with previous findings (*25*), with a bias of less than 10%–15% compared with BP_{ND}, although overall the latter (110–130 min) interval performed slightly better. The observed linearity between SUVR and BP_{ND} suggests that SUVR would provide robust estimates across levels of tau for cross-sectional or longitudinal imaging studies, although further studies with dynamic image acquisition may be warranted to confirm the linearity of the relationship across a wider range of tau load. In this study, other factors such as the

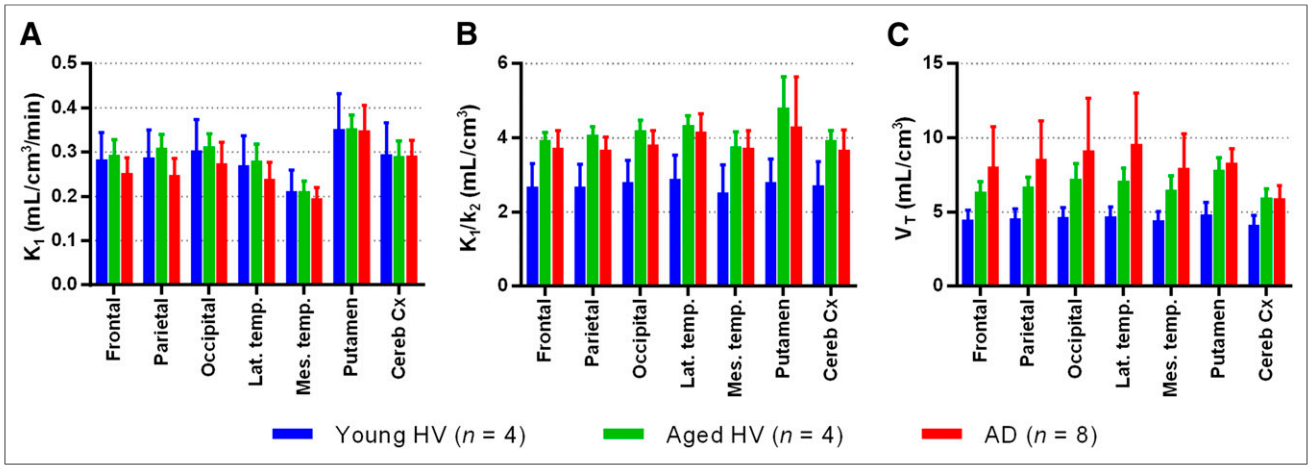

FIGURE 5. 2T parameters using 130 min of scanning data. Values are mean ± SD within each group. Average of left and right regions; frontal = average of inferior, superior, and middle; lateral temporal = average of superior and inferior.

SUVR reproducibility at different time intervals or its sensitivity to blood flow were not taken into consideration. The impact of regional cerebral blood flow changes, likely to happen in AD (*26*), on SUVR but also BP_{ND}, needs further investigation through computer simulations, BP_{ND} being likely less sensitive but requiring dynamic data acquisition not always feasible in clinical studies. Additionally, our results highlight the time dependence of SUVR (Fig. 7D), and the scan imaging time should be controlled, particularly in longitudinal or drug-development studies, so that additional variability in ΔSUVR assessments is not introduced.

A different kinetic profile was observed in the putamen, globus pallidus, and thalamus compared with cortical regions (Supplemental Figs. 5 and 6), suggesting that ^{18}F-AV-1451 may bind to a different site in these regions, with a higher (about double) k_4 than in cortical regions (Table 2). Furthermore, similar to our findings of elevated signal in the putamen and globus pallidus in AHVs and AD subjects compared with YHVs, an increased SUVR in older subjects was recently reported (*27*) where it was hypothesized that the higher uptake was due to an increased capillary permeability in the putamen and globus pallidus, but not in the cerebellar cortex. An increased capillary permeability would imply an increased extraction and in turn, under passive transport condition through the blood–brain barrier, an increased K_1 and k_2 that would produce an initial higher uptake (higher K_1) followed by a faster washout (higher k_2). However, our kinetic modeling results showed similar K_1 across the 3 groups in the putamen and cerebellar cortex with, on the other hand, a lower k_2 (higher K_1/k_2) in AHVs and AD subjects compared with YHVs.

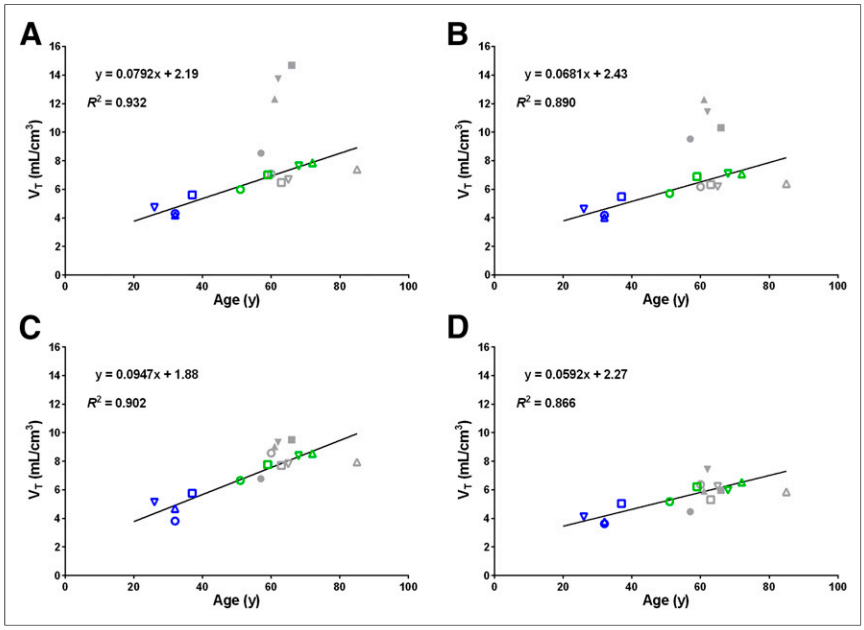

FIGURE 6. Linear regression of V_T (2T, 130 min) against subject's age in lateral temporal cortex (A), parietal cortex (B), putamen (C), and cerebellar cortex (D). Blue symbols = YHV; green symbols = AHV; solid line = linear regression. AD (gray symbols) were excluded from regression analysis and are shown for information only: open symbols = Mini-Mental State Examination > 25 (low tau signal), closed symbols = Mini-Mental State Examination < 25.

V_T was increased in AHVs and AD subjects not solely in the putamen but in all brain regions investigated, including the cerebellar cortex (Fig. 5; Table 2). Furthermore, this increase was found to be age dependent (Fig. 6). This age-dependent V_T increase appears through the k_2 parameter (negative correlation), although because of parameter identifiability (correlation between k_2 and k_3) (*24*), it was more pronounced for V_T. Although the age dependency mostly normalized out when calculating SUVR or BP_{ND} with, for instance, a remaining correlation between the subject's age and SUVR (80–100 min) of $R^2 = 0.79$ in the putamen ($P < 0.001$, increase of 0.0060/y) and of $R^2 = 0.31$ in the lateral temporal cortex (not significant, $P = 0.1$; increase of 0.0017/y), these findings suggest that HVs should be age-matched with AD subjects when using SUVR or BP_{ND} because V_T increased in the cerebellar cortex. One interpretation of these results would be of an age-dependent

TABLE 3
Linear Regression Analysis of BP_{ND} and SUVR Estimates Across Methods and Scanning Duration (130 and 210 Minutes) in AD (n = 8)

Method	Parameter	2T	LGA	NI-LGA	SUVR-1 (80–100)	SUVR-1 (110–130)
2T	Slope	1.146	—	—	—	—
	Intercept	0.009	—	—	—	—
	R^2	0.95	—	—	—	—
LGA	Slope	0.929	1.103	—	—	—
	Intercept	0.002	0.003	—	—	—
	R^2	0.98	0.98	—	—	—
NI-LGA	Slope	0.815	0.887	1.123	—	—
	Intercept	0.007	0.007	0.005	—	—
	R^2	0.97	0.99	0.99	—	—
SUVR-1 (80–100)	Slope	0.872	0.943	1.069	—	—
	Intercept	0.082	0.092	0.083	—	—
	R^2	0.97	0.96	0.97	—	—
SUVR-1 (110–130)	Slope	1.088	1.145	1.289	1.204	—
	Intercept	0.081	0.089	0.080	−0.009	—
	R^2	0.97	0.98	0.98	0.99	—
SUVR-1 (160–180)	Slope	1.223	1.295	1.456	1.334	1.119
	Intercept	0.068	0.075	0.066	−0.036	−0.020
	R^2	0.96	0.97	0.97	0.96	0.97

Below diagonal: column heading as abscissa and row heading as ordinate for 130-min estimates for 2T, LGA, and NI-LGA. Diagonal: within method (2T, LGA, and NI-LGA) comparison, 130-min estimates as abscissa and 210-min estimates as ordinate.

increase of nonspecific signal or binding to a secondary target not kinetically separated from the nondisplaceable signal, although it is not clear what a widespread secondary binding increasing with age would be. Another interpretation would be a change of the tracer efflux to plasma (*27*), although this would imply some transport mechanism through the blood–brain barrier other than passive diffusion.

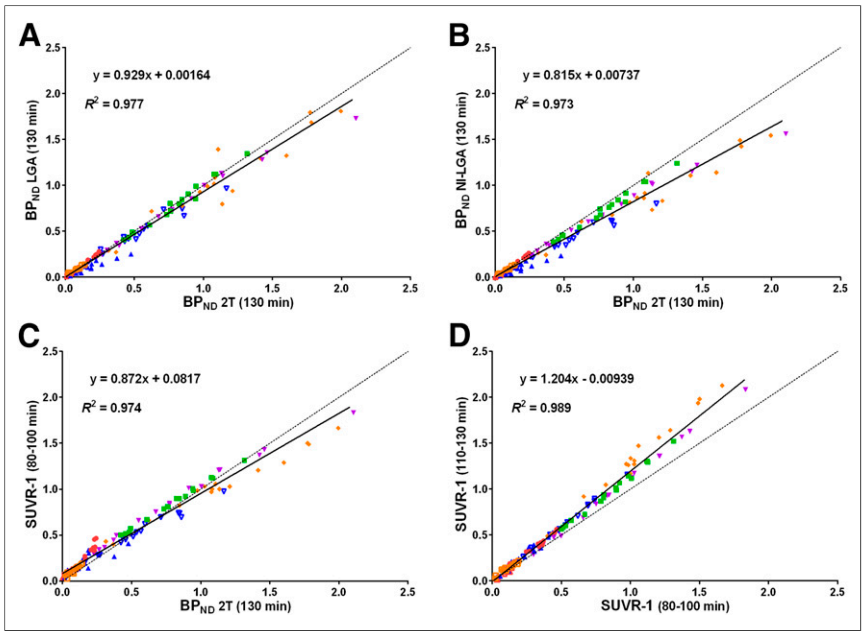

FIGURE 7. Regression analysis in AD (n = 8) between BP_{ND} 2T (130 min) and BP_{ND} LGA (130 min) (A), BP_{ND} NI-LGA (130 min) (B), and SUVR-1 (80–100 min) (C), and between SUVR-1 (80–100 min) and SUVR-1 (110–130) (D). Colors indicate different subjects; solid line = linear regression; dashed line = line of identity.

CONCLUSION

^{18}F-AV-1451 retention is currently assessed in clinical studies of AD at 80–100 min after injection. Simplified methods of image acquisition or analysis often require a trade-off between accuracy and simplicity, and given the good correlation between BP_{ND} and SUVR-1, our data suggest that SUVR estimates in this imaging window provide information of tau burden, with an underestimation of 10%–15% for higher tau load, although the later imaging window of 110–130 min performed slightly better. Consideration should be given to imaging time in longitudinal or drug-development studies so that additional variability in the assessment of tau load changes is not introduced, and SUVR sensitivity to changes in regional cerebral blood or clearance should be further investigated.

DISCLOSURE

This study was sponsored by Molecular Neuroimaging, a division of inviCRO, and

funded by Roche. Olivier Barret, David Alagille, Caroline Papin, Thomas Morley, Ken Marek, John P. Seibyl, Gilles D. Tamagnan, and Danna Jennings are employees of Molecular Neuroimaging. Robert A. Comley, Edilio Borroni, and Nicholas Seneca are employees of Roche; Sandra Sanabria and Robby M. Weimer are employees of Genentech; and Mark Mintun is employee of Avid. No other potential conflict of interest relevant to this article was reported.

ACKNOWLEDGMENT

We thank Julie C. Price for reading the manuscript and providing suggestions.

REFERENCES

1. Braak H, Braak E. Neuropathological stageing of Alzheimer-related changes. *Acta Neuropathol (Berl).* 1991;82:239–259.
2. Chien DT, Bahri S, Szardenings AK, et al. Early clinical PET imaging results with the novel PHF-tau radioligand [F-18]-T807. *J Alzheimers Dis.* 2013;34:457–468.
3. Xia CF, Arteaga J, Chen G, et al. [^{18}F]T807, a novel tau positron emission tomography imaging agent for Alzheimer's disease. *Alzheimers Dement.* 2013;9: 666–676.
4. Marquié M, Normandin MD, Vanderburg CR, et al. Validating novel tau positron emission tomography tracer [F-18]-AV-1451 (T807) on postmortem brain tissue. *Ann Neurol.* 2015;78:787–800.
5. Wood H. Alzheimer disease: [^{11}C]PBB3—a new PET ligand that identifies tau pathology in the brains of patients with AD. *Nat Rev Neurol.* 2013;9:599.
6. Maruyama M, Shimada H, Suhara T, et al. Imaging of tau pathology in a tauopathy mouse model and in Alzheimer patients compared to normal controls. *Neuron.* 2013;79:1094–1108.
7. Okamura N, Furumoto S, Harada R, et al. Novel ^{18}F-labeled arylquinoline derivatives for noninvasive imaging of tau pathology in Alzheimer disease. *J Nucl Med.* 2013;54:1420–1427.
8. Chien DT, Szardenings AK, Bahri S, et al. Early clinical PET imaging results with the novel PHF-tau radioligand [F18]-T808. *J Alzheimers Dis.* 2014;38:171–184.
9. Muhs A, Berndt M, Kroth H, et al. Characterization and development of novel tau PET tracers for the assessment of tau spreading in Alzheimer's disease. Paper presented at: the 8th Clinical Trials on Alzheimer's Disease; November 5–7, 2015; Barcelona, Spain.
10. Wong DF, Borroni E, Kuwabara H, et al. First in-human PET study of 3 novel tau radiopharmaceuticals: [^{11}C]RO6924963, [^{11}C]RO6931643, and [^{18}F]RO6958948. *Alzheimers Dement.* 2015;11: P850–P851.
11. Harada R, Okamura N, Furumoto S, et al. ^{18}F-THK5351: a novel PET radiotracer for imaging neurofibrillary pathology in Alzheimer disease. *J Nucl Med.* 2016;57: 208–214.
12. Sanabria Bohorquez S, Barret O, Tamagnan G, et al. Quantification, test-retest and dosimetry of the novel Genentech tau probe 1, [^{18}F]GTP1. Paper presented at: the 10th Human Amyloid Imaging; January 13–15, 2016; Miami, Florida.
13. Walji AM, Hostetler ED, Selnick H, et al. Discovery of 6-(Fluoro-^{18}F)-3-(^{1}H-pyrrolo[2,3-c]pyridin-1-yl)isoquinolin-5-amine ([^{18}F]-MK-6240): a positron emission tomography (PET) imaging agent for quantification of neurofibrillary tangles (NFTs). *J Med Chem.* 2016;59:4778–4789.
14. Choi JY, Lyoo CH, Lee JH, et al. Human radiation dosimetry of [^{18}F]AV-1451 (T807) to detect tau pathology. *Mol Imaging Biol.* 2016;18:479–482.
15. Shcherbinin S, Schwarz AJ, Joshi A, et al. Kinetics of the tau PET tracer ^{18}F-AV-1451 (T807) in subjects with normal cognitive function, mild cognitive impairment, and Alzheimer disease. *J Nucl Med.* 2016;57:1535–1542.
16. Shoup TM, Yokell DL, Rice PA, et al. A concise radiosynthesis of the tau radiopharmaceutical, [^{18}F]T807. *J Labelled Comp Radiopharm.* 2013;56:736–740.
17. McKhann GM, Knopman DS, Chertkow H, et al. The diagnosis of dementia due to Alzheimer's disease: recommendations from the National Institute on Aging-Alzheimer's Association workgroups on diagnostic guidelines for Alzheimer's disease. *Alzheimers Dement.* 2011;7:263–269.
18. Schreiber S, Landau SM, Fero A, Schreiber F, Jagust WJ, Alzheimer's Disease Neuroimaging Initiative. Comparison of visual and quantitative florbetapir F 18 positron emission tomography analysis in predicting mild cognitive impairment outcomes. *JAMA Neurol.* 2015;72:1183–1190.
19. Hammers A, Allom R, Koepp MJ, et al. Three-dimensional maximum probability atlas of the human brain, with particular reference to the temporal lobe. *Hum Brain Mapp.* 2003;19:224–247.
20. Innis RB, Cunningham VJ, Delforge J, et al. Consensus nomenclature for in vivo imaging of reversibly binding radioligands. *J Cereb Blood Flow Metab.* 2007;27: 1533–1539.
21. Logan J. Graphical analysis of PET data applied to reversible and irreversible tracers. *Nucl Med Biol.* 2000;27:661–670.
22. Lammertsma AA, Hume SP. Simplified reference tissue model for PET receptor studies. *Neuroimage.* 1996;4:153–158.
23. Trollor JN, Sachdev PS, Haindl W, Brodaty H, Wen W, Walker BM. Regional cerebral blood flow deficits in mild Alzheimer's disease using high resolution single photon emission computerized tomography. *Psychiatry Clin Neurosci.* 2005;59:280–290.
24. Koeppe RA, Frey KA, Vander Borght TM, et al. Kinetic evaluation of [^{11}C] dihydrotetrabenazine by dynamic PET: measurement of vesicular monoamine transporter. *J Cereb Blood Flow Metab.* 1996;16:1288–1299.
25. Baker S, Price JC, Lockhart SN, et al. Reference tissue-based kinetic evaluation of [F-18]AV-1451 in aging and dementia. Paper presented at: the 12th International Conference on Quantification of Brain Function with PET; June 27–30, 2015; Vancouver, Canada.
26. van Berckel BN, Ossenkoppele R, Tolboom N, et al. Longitudinal amyloid imaging using ^{11}C-PiB: methodologic considerations. *J Nucl Med.* 2013;54: 1570–1576.
27. Pascual B, Rockers E, Bajaj S, et al. Regional kinetics of [^{18}F]AV-1451 uptake and gadolinium concentration in young and older subjects. Paper presented at: the 10th Human Amyloid Imaging; January 13–15, 2016; Miami, Florida.